ROYAL SOCIETY
OF CHEMISTRY

PAPER

Check for updates

White light tuning and temperature sensing of NaLu(WO$_4$)$_2$:Ln^{3+} up-converting phosphor

Zhiyi Wang,†[a] Li Jiang,†[a] Dongmei Wang,[a] Jie Cheng,[b] Jingjing li,[b] Yanhan Mei,[b] Shanshan Hu*[a] and Jun Yang [ID] *[a]

NaLu(WO$_4$)$_2$:Ln^{3+} phosphors were synthesized *via* a hydrothermal method combined with subsequent calcination. Under excitation at 980 nm, 25%Yb^{3+}, 0.5%Tm^{3+} and 25%Yb^{3+}, 1%Ho^{3+}-doped phosphors produce blue, green and red emissions. Namely, NaLu(WO$_4$)$_2$:25%Yb^{3+}, 0.1%Ho^{3+}, 0.1%Tm^{3+} nanocrystals show suitable intensities of blue, green, and red (RGB) emission, resulting in the production of perfect and bright white light with CIE-x = 0.3299 and CIE-y = 0.3293, which is very close to the standard equal energy white light illumination (x = 0.33, y = 0.33). Based on FIR theory, the temperature dependence of NaLu(WO$_4$)$_2$:20%Yb^{3+}, 1%Er^{3+} was studied, and the maximum value of sensitivity was obtained as 1.38% K^{-1} at 543 K, which is better than that of previously reported temperature-sensing materials. It proves that the NaLu(WO$_4$)$_2$:Ln^{3+} phosphors have potential applications in white lighting, optical temperature measurement and other fields.

Introduction

In recent years, rare earth (RE) tungstates have been favored by a large number of researchers because of their excellent theoretical density and remarkable resistance to thermal, chemical, mechanical and optical damage. So far, these compounds are used in optical imaging, biological nanothermometers, LEDs, optical nanothermometers and dye-sensitized solar cells.[1–5] RE double tungstates (ARE(WO$_4$)$_2$, A = alkali metal) are widely studied due to their excellent physical and chemical stability owing to their special scheelite structure. Hence, a lot of effort has recently been invested in the synthesis of Lu^{3+}, La^{3+}, Y^{3+} and Gd^{3+}-based rare earth double tungstates, which have a controlled crystal shape, phase and size.[4,6–8] Lu^{3+} in particular, which is located at the end of the rare earth elements and whose 4f orbital is fully filled with electrons, is widely regarded as an outstanding phosphorus matrix tungstate. Shi's team produced NaLu(WO$_4$)$_2$·2H$_2$O by a hydrothermal reaction of Na$_2$WO$_4$·2H$_2$O and Lu(NO$_3$)$_3$ and investigated the up/down conversion luminescence characteristics of the NaLu(WO$_4$)$_2$:Yb/Ln (Ln = Er, Ho, Tm) phosphor.[6] Nexha *et al.*[9] prepared Ho,Tm-doped KLu(WO$_4$)$_2$ nanocrystals through a modified sol–gel method, controlled the amount of doped ions to obtain different regular shapes of nanocrystals with a size of about 150 nm and explored the temperature dependence in the temperature range of 293 to

333 K under short-wave infrared excitation. Barrera *et al.*[10] synthesized KLu(WO$_4$)$_2$:Yb^{3+}, Tm^{3+}, Ho^{3+} nanocrystals *via* an improved Pechini sol–gel method and studied the effect of Eu doping on the white light up-conversion of Yb-sensitized KLu(WO$_4$)$_2$:Ho^{3+}, Tm^{3+} nanocrystals. The matrix material selected in this paper is NaLu(WO$_4$)$_2$, which will be an excellent candidate for temperature measurement and white light production.[3,6,11]

RE doped up-conversion (UC) luminescence is an anti-Stokes process, which emits high-energy visible light under low-energy infrared excitation.[12,13] So far, UC phosphors have been widely used in many fields and have developed rapidly. Recently, researchers have considered Yb^{3+}/Er^{3+}-doped up-conversion phosphors as candidates for optical temperature measurement.[2,14] The importance of temperature in chemical reactions is self-evident and the accurate understanding of temperature change is extremely critical. There are various techniques for measuring temperature. In addition to traditional temperature measurement techniques, thermistors or thermocouples are also widely used. Optical thermometry based on UC phosphors is different from traditional thermometry.[4,14,15] It is a non-contact temperature measurement method that has excellent thermal sensitivity and strong adaptive abilities. The principle of non-contact optical temperature measurement technology is based on the variation of the relative intensity of the emission band between two adjacent thermal coupling energy levels (^{2}H$_{11/2}$ and ^{4}S$_{3/2}$) of Er^{3+} with temperature.[12] Up to now, Yb^{3+}/Er^{3+}-doped UC phosphors, involving oxides, fluorides, tungstates and molybdates, are very popular in the field of optical temperature measurement.[4,14,16–20] Compared with other compounds, tungstates have the advantages of simple

[a]School of Chemistry and Chemical Engineering, Southwest University, No. 2 Tiansheng Road, Beibei District, Chongqing 400715, China. E-mail: hushan3@swu.edu.cn; jyang@swu.edu.cn

[b]Chongqing Songshuqiao Middle School, Chongqing 401147, China

† These authors contributed equally to this work.

preparation, outstanding physical, thermal and chemical stability, controllable size and morphology, *etc.* Therefore, they have general application prospects in the field of optical temperature measurement.

In recent decades, RE-doped UC white emission materials have attracted great attention due to their advantages of high energy efficiency, long life, low cost, and pro-environment nature.[21] Based on the principle of the three primary colors, white light can be produced by mixing red, green and blue in a suitable ratio.[21–24] Among the RE elements, Tm^{3+} is the most popular because of its blue and red emission bands.[25,26] In the same material, UC white light is frequently obtained *via* triple-doping Yb^{3+}, Ho^{3+} (Er^{3+}), and Tm^{3+} in an appropriate mixing ratio. Mèndez-Ramos and colleagues prepared $YF_3:Ln^{3+}$ (Ln = Yb, Ho, Tm) phosphors *via* heat treatment of a sol–gel glass precursor, and obtained standard bright UC white light by controlling the doping ion concentration.[27] Xu's group used a microwave hydrothermal method to synthesize the $NaGd(WO_4)_2:Yb^{3+}/Ho^{3+}/Tm^{3+}$ phosphor, and added glycerin to change the particle size. Under near-infrared excitation, the $NaGd(WO_4)_2:Yb^{3+}/Ho^{3+}/Tm^{3+}$ phosphor showed red, green, and blue emission at the same time with white light.[28] However, so far there has been almost no report on the UC white emission of $NaLu(WO_4)_2:Ln^{3+}$.

In this work, we successfully synthesized the $NaLu(WO_4)_2$:Ln^{3+} phosphor through a simple hydrothermal method and subsequent calcination. Under near infrared (NIR) excitation, the $NaLu(WO_4)_2:Yb^{3+}/Er^{3+}$ phosphor presented green emission, which was detected in the temperature range of 323–523 K and the maximum sensitivity was calculated; the standard white UC luminescence was obtained by triple-doping an appropriate atomic ratio of Yb^{3+}, Ho^{3+} and Tm^{3+}.

Experiments

Materials

Sodium tungstate (Na_2WO_4, AR), sodium hydroxide (NaOH, AR), nitric acid (HNO_3, AR), lutetium oxide (Lu_2O_3, 99.99%), ytterbium oxide (Yb_2O_3, 99.99%), erbium oxide (Er_2O_3, 99.99%), holmium oxide (Ho_2O_3, 99.99%) and thulium oxide (Tm_2O_3, 99.99%) were used as raw materials. None of the materials were further purified. Lu_2O_3, Yb_2O_3, Er_2O_3, Ho_2O_3 and Tm_2O_3 were dissolved in concentrated nitric acid with heating and stirring until completely dissolved, excess nitric acid was evaporated at high temperature and finally diluted and cooled to obtain $Lu(NO_3)_3$, $Yb(NO_3)_3$, $Er(NO_3)_3$, $Ho(NO_3)_3$ and $Tm(NO_3)_3$ solutions, respectively.

Synthesis of $NaLu(WO_4)_2:Ln^{3+}$

$NaLu(WO_4)_2:Ln^{3+}$ phosphors were prepared *via* a typical hydrothermal method with further calcination. The $Ln(NO_3)_3$ (Ln = Lu/Yb/Er/Ho/Tm) solution was added dropwise to 35 ml distilled water at room temperature, and stirred with a strong magnetic force for half an hour. Then, Na_2WO_4 was added to the above mixed solution, the pH of the mixed solution was adjusted to 8 with HNO_3 or NaOH and stirred to obtain a white

colloid. After 30 min, the colloid was transferred to a reaction kettle for a 200 °C thermostat reaction for 12 h. Subsequently, the reaction mixture was cooled to room temperature and centrifuged, washed repeatedly with deionized water and ethanol, and dried at 70 °C for 12 h. Finally, it was evenly ground and calcined at 600 °C for 2 h to obtain the product.[6]

Characterization

The crystal phase was detected using equipment ($MSALXD_3$, using Cu Kα radiation ($\lambda = 0.15405$ nm)) provided by Beijing General Analysis General Instrument Co. The emission current and acceleration voltage are 20 mA and 26 kV, respectively. Additionally, the scanning range of 2θ is from 10° to 90°. The crystal morphology was analyzed using scanning electron microscopy (SEM, model S-4800) manufactured by Hitachi, Japan, with an acceleration voltage of 10 kV. A PerkinElmer instrument (model MDL-N-980-8W, ls55) was used to analyze the UC spectrum and temperature dependence of the wavelength from 400 to 750 nm.

Results and discussion

Structural analysis

Fig. 1a displays the XRD patterns of $NaLu(WO_4)_2$ and $NaLu(WO_4)_2:Ln^{3+}$. All diffraction peaks can be as attributed to the pure tetragonal $NaLu(WO_4)_2$ phase, highly compatible with the standard cards (JCPDS no. 27-0729). No additional diffraction peaks are detected, showing that high purity products are synthesized and that the Ln^{3+} ions (Ln = Yb, Er, Ho, Tm) were fully dissolved into $NaLu(WO_4)_2$ host. Moreover, the sharp diffraction peaks indicate the high crystallinity of the products, which signifies high luminous intensity. The ion radius of doped Ln^{3+} ($r(Yb^{3+}) = 0.86$ Å, $r(Er^{3+}) = 0.88$ Å, $r(Ho^{3+}) = 0.89$ Å, $r(Tm^{3+}) = 0.87$ Å) is larger than that of Lu^{3+} ($r(Lu^{3+}) = 0.85$ Å), which leads to lattice expansion, and the diffraction peaks are slightly shifted to smaller 2θ values, as shown in Fig. 1b. It is worth noting that the XRD peaks of (112), (204) and (312) increase with Ln^{3+} doping, which indicates that larger radius ion doping is more likely to form smaller nanocrystals.[29]

In general, the subsequent calcination temperature does not change the morphology of the product derived from its corresponding hydrothermal precursor. Fig. 2 displays the SEM morphologies of the calcined products with different doped ions at 600 °C. Ln^{3+} doping has little effect on crystal

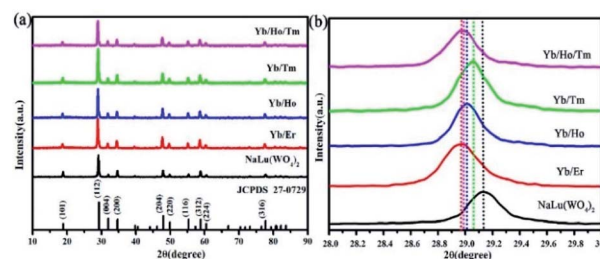Fig. 1 (a) XRD patterns of pure $NaLu(WO_4)_2$ and $NaLu(WO_4)_2:Ln^{3+}$. (b) Enlarging the main diffraction peak of (112) from (a).
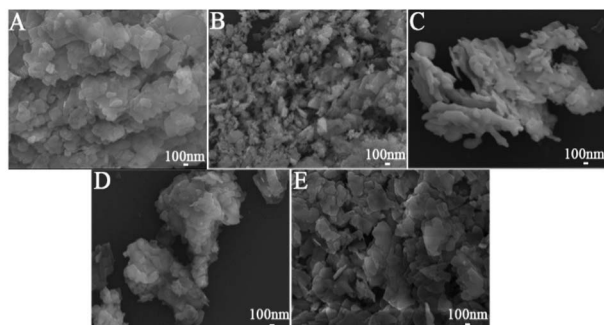
© 2022 The Author(s). Published by the Royal Society of Chemistry

Fig. 2 SEM of different doped ions of the products calcined at 600 °C: (a) NaLu(WO$_4$)$_2$, (b) NaLu(WO$_4$)$_2$:20%Yb^{3+}, 1%Er^{3+}, (c) NaLu(WO$_4$)$_2$:25%Yb^{3+}, 1%Ho^{3+}, (d) NaLu(WO$_4$)$_2$:25%Yb^{3+}, 0.5%Tm^{3+} and (e) NaLu(WO$_4$)$_2$:25%Yb^{3+}, 0.1%Ho^{3+}, 0.1%Tm^{3+}.

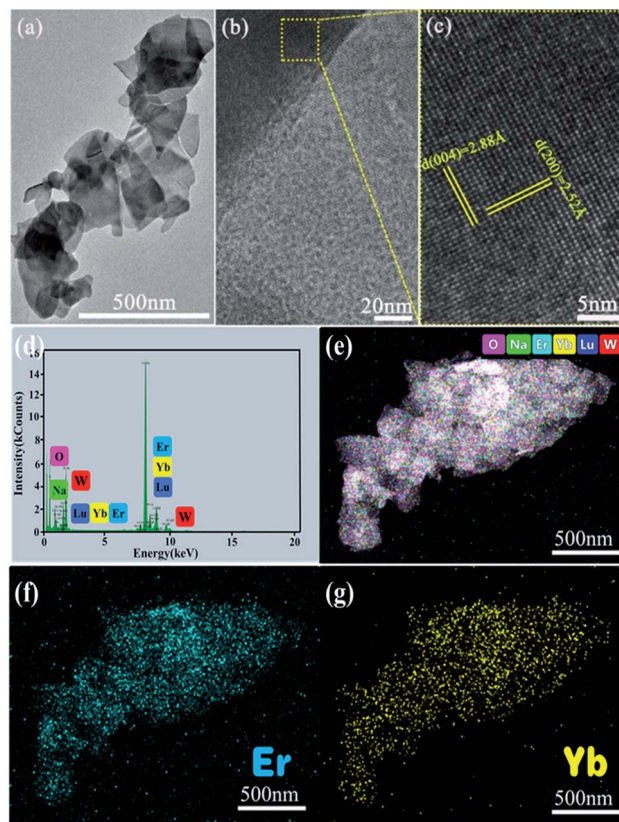**Fig. 3** (a) TEM morphology, (b) HR-TEM lattice fringes, (c) the magnification of (b) for NaLu(WO$_4$)$_2$, (d) EDS spectrum, (e) mapping analysis, (f) distribution density map of Er and (g) distribution density map of Yb.

morphology, but the particle size decreases slightly. The size of the NaLu(WO$_4$)$_2$ nanocrystals decreases slightly with varying Ln^{3+} ion radius, which is also consistent with the XRD analysis result of Fig. 1b. A larger dopant ion radius can reduce the anisotropic growth rate of the crystal grains, which is the main reason for the size change of the NaLu(WO$_4$)$_2$:Ln^{3+} nanocrystals. When Ln^{3+} with a larger ionic radius replaces Lu^{3+}, the exposed charge density of the NaLu(WO$_4$)$_2$ nanocrystals increases. The exposed charge density of the nanocrystals can significantly slow down the movement of the negatively charged WO$_4{}^{2-}$ ions to the surface due to the increase in charge repulsion, which leads to decrease size in the NaLu(WO$_4$)$_2$:Ln^{3+} nanocrystals.[29–31]

TEM analysis depicts nanosheets of the NaLu(WO$_4$)$_2$ crystals with a diameter of about 200–300 nm (Fig. 3a), which corresponds to the nanoplatelets observed in Fig. 2a. HR-TEM analysis (Fig. 3b and c) showed distinguishable lattice fringes with interplanar spacings of 2.88 Å and 2.52 Å, which can be classified as the (004) and (200) planes of tetragonal NaLu(WO$_4$)$_2$, respectively. In order to further prove the successful doping and uniform distribution of Yb^{3+} and Er^{3+} in the NaLu(WO$_4$)$_2$ matrix, we performed EDS tests and mapping analysis. The results are shown in Fig. 3d–e. In Fig. 3d, we can see that Na, Lu, Yb, Er, W and O elements are all detected in the product, which is consistent with the XRD results above. The overall distribution of various elements as well as Yb and Er in the product is shown in Fig. 3e–g, and the elements corresponding to different colors are shown in the upper right corner of Fig. 3e. Namely, we achieved uniform doping of Yb^{3+} and Er^{3+} in the NaLu(WO$_4$)$_2$ matrix, which provides support for us to explore the luminescence characteristics of the product in later experiments.

Luminescence of the NaLu(WO$_4$)$_2$:Ln^{3+} phosphors

Fig. 4a shows the UC emission spectrum (400–750 nm) of NaLu(WO$_4$)$_2$:Ln^{3+} nanocrystals under excitation at 980 nm. The UC emission spectra of NaLu(WO$_4$)$_2$:25%Yb^{3+}, 0.5%Tm^{3+} depicts strong blue emission at 475 nm and weak red emission at 647 nm, which are attributed to the $^1G_4 \rightarrow {}^3H_6$ and $^1G_4 \rightarrow {}^3F_4$ transitions of Tm^{3+}, respectively. The emission spectrum of NaLu(WO$_4$)$_2$:25%Yb^{3+}, 1%Ho^{3+} displays green emission that is

mainly located at 539 nm due to the $^5F_4/{}^5S_2 \rightarrow {}^5I_8$ transition of Ho^{3+} ions, and the red emission located at 658 nm is caused by the $^5F_5 \rightarrow {}^5I_8$ radiation transition of Ho^{3+} ions. The chromaticity coordinates of the NaLu(WO$_4$)$_2$:25%Yb^{3+}, 0.5%Tm^{3+} and NaLu(WO$_4$)$_2$:25%Yb^{3+}, 1%Ho^{3+} phosphors are (0.1798, 0.1459) and (0.4108, 0.4334), respectively (Fig. 4b), which is consistent with the luminescent photographs obtained under excitation (insets in Fig. 4a).

Based on the generation of red, green, and blue emissions in the different doped NaLu(WO$_4$)$_2$:Ln^{3+} nanocrystals, it is possible to produce luminescence with a wide spectrum of colors, including white, by the appropriate doping of Yb^{3+}, Tm^{3+}, and Ho^{3+} in the present NaLu(WO$_4$)$_2$ nanocrystals.

Fig. 5a displays the UC emission spectrum of NaLu(WO$_4$)$_2$:25%Yb^{3+}, 0.1%Ho^{3+}, y%Tm^{3+} phosphors. It can be observed that the UC emission spectrum of the phosphors are composed of blue emission, green emission and red emission, which are attributed to the $^1G_4 \rightarrow {}^3H_6$ transition of Tm^{3+} and the $^5F_4/{}^5S_2 \rightarrow {}^5I_8$ and $^5F_5 \rightarrow {}^5I_8$ radiation transitions of Ho^{3+}, respectively. The CIE chromaticity coordinates of NaLu(WO$_4$)$_2$:25%Yb^{3+}, 0.1%Ho^{3+}, y%Tm^{3+} phosphors alter from the blue-white area (0.317, 0.3078) to the white area (0.3299, 0.3293) by changing the Tm^{3+} doping content (as shown in Fig. 5b). In addition, the white UC photoluminescence
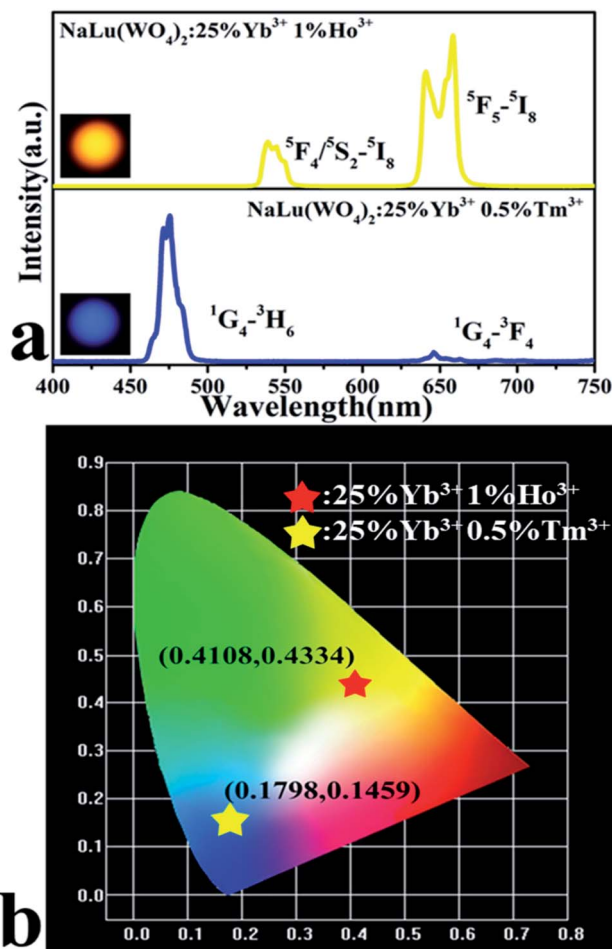
Fig. 4 (a) UC emission spectra and the corresponding luminescence photos of the $NaLu(WO_4)_2$:25%Yb^{3+}, 1%Ho^{3+} and $NaLu(WO_4)_2$:25%Yb^{3+}, 0.5%Tm^{3+} nanocrystals under excitation at 980 nm; (b) the chromaticity coordinates of $NaLu(WO_4)_2$:25%Yb^{3+}, 1%Ho^{3+} and $NaLu(WO_4)_2$:25%Yb^{3+}, 0.5%Tm^{3+}.
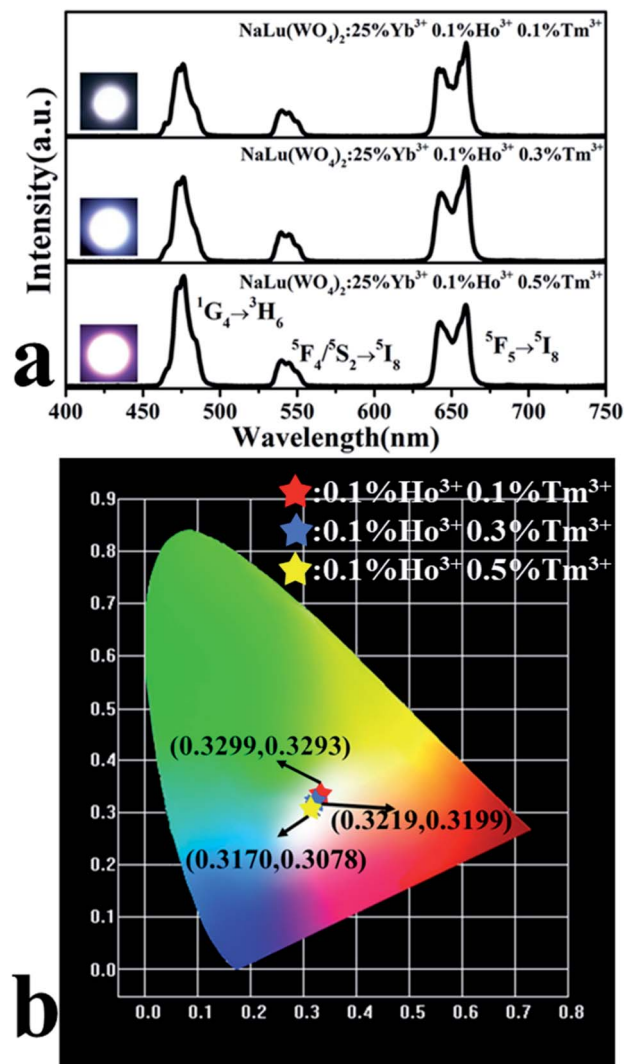

Fig. 5 (a) UC emission spectra of the $NaLu(WO_4)_2$:25%Yb^{3+}, 0.1%Ho^{3+}, y%Tm^{3+} nanocrystals under excitation at 980 nm ($y = 0.1$, 0.3 and 0.5); (b) the chromaticity coordinates of $NaLu(WO_4)_2$:25%Yb^{3+}, 0.1%Ho^{3+}, y%Tm^{3+} ($y = 0.1$, 0.3 and 0.5).

of the $NaLu(WO_4)_2$ phosphor is obtained at $y = 0.1$ and its corresponding chromaticity coordinates (0.3299, 0.3293) are almost equivalent to the international standard values (0.33, 0.33). Simultaneously, the corresponding white UC luminescence photographs are also presented in the inset of Fig. 5a, which can be intuitively compared.

As we all know, the functional relationship between the UC emission intensity (I) and the laser pump power (P) can be described as $I \propto P^n$, where n represents the number of laser photons.[25,28] The value of n is derived from the slope obtained by fitting P and I (Fig. 6a). The n values of blue, green, and red emissions are 2.41, 2.00, and 1.79, respectively. It is concluded that the blue emission is assigned to the three-photon process, and the green and red emission are attributed to the two-photon process. The UC luminescence mechanism of $NaLu(WO_4)_2$:25% Yb^{3+}, 0.1%Ho^{3+}, 0.1%Tm^{3+} was deduced from the above results (as shown in Fig. 6b). Under excitation at 980 nm, the electrons of Yb^{3+} are filled from $^2F_{7/2}$ to $^2F_{5/2}$ by absorbing phonon energy. In the meantime, the electrons of the Ho^{3+} and Tm^{3+} activator

ions are populated from $^5I_8$ and $^3H_6$ to $^5I_6$ and $^3H_5$, respectively ($^2F_{5/2}$ (Yb^{3+}) + $^5I_8$ (Ho^{3+}) → $^2F_{7/2}$ (Yb^{3+}) + $^5I_6$ (Ho^{3+}); $^2F_{5/2}$ (Yb^{3+}) + $^3H_6$ (Tm^{3+}) → $^2F_{7/2}$ (Yb^{3+}) + $^3H_5$ (Tm^{3+})). For Ho^{3+} ions, after the non-radiative transition of Ho^{3+} from $^5I_6$ to $^5I_7$, the Ho^{3+} ions are excited from $^5I_7$ to $^5F_5$ ($^2F_{5/2}$ (Yb^{3+}) + $^5I_7$ (Ho^{3+}) → $^2F_{7/2}$ (Yb^{3+}) + $^5F_5$ (Ho^{3+})). The radiative release of Ho^{3+} ions from $^5F_5$ to $^5I_8$ generates the red emission (659 nm). Subsequently, the further transitions of Ho^{3+} from $^5I_6$ to $^5F_4$, $^5S_2$ $^2F_{5/2}$ (Yb^{3+}) + $^5I_6$ (Ho^{3+}) → $^2F_{7/2}$ (Yb^{3+}) + $^5F_4$, $^5S_2$ (Ho^{3+}) occur, and the green emission (544.5 nm) is obtained by the radiative release of Ho^{3+} ($^5F_4$, $^5S_2$ → $^5I_8$). For Tm^{3+} ions, the non-radiative relaxation to the $^3F_4$ and $^3H_4$ levels ($^3H_5$ → $^3F_4$ and $^3F_3$ → $^3H_4$), and the subsequent excitation transitions of the $^3F_4$ and $^3H_4$ levels to the $^3F_3$ and $^1G_4$ levels occur ($^2F_{5/2}$ (Yb^{3+}) + $^3F_4$ (Tm^{3+}) → $^2F_{7/2}$ (Yb^{3+}) + $^3F_3$ (Tm^{3+}) and $^2F_{5/2}$ (Yb^{3+}) + $^3H_4$ (Tm^{3+}) → $^2F_{7/2}$(Yb^{3+}) + $^1G_4$ (Tm^{3+})). Finally, the blue emission (476.5 nm) is afforded via the radiative relaxation from $^1G_4$ to the $^3H_6$ level.
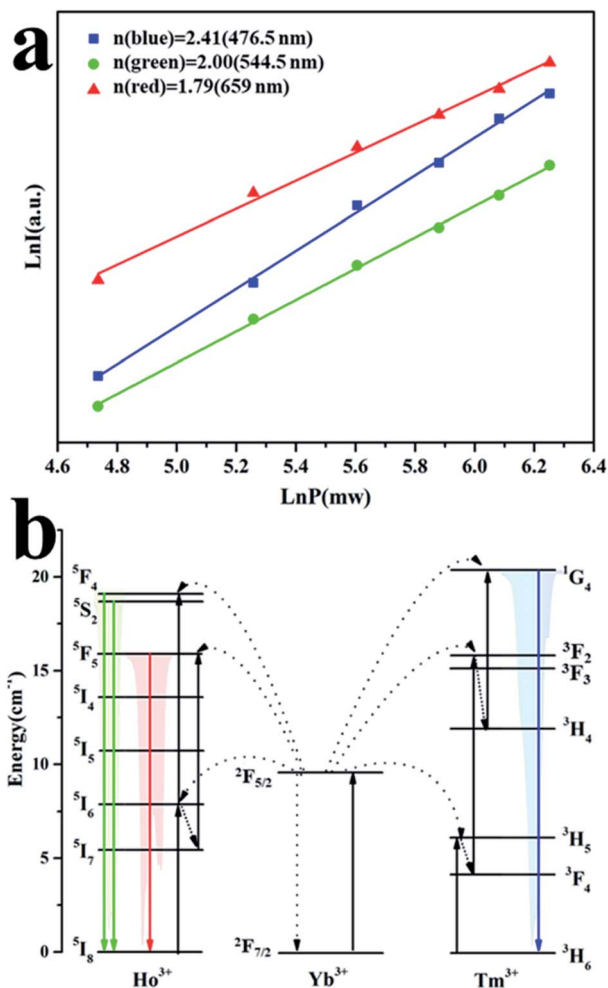
Fig. 6 (a) Functional relationship between LnI and LnP, (b) UC mechanism of NaLu(WO$_4$)$_2$:25%Yb^{3+}, 0.1%Ho^{3+}, 0.1%Tm^{3+}.

Temperature sensing behavior and temperature sensing performance

Considering the absorption cross section and the significant difference in concentration between Yb^{3+} and Er^{3+}, the UC mechanism of NaLu(WO$_4$)$_2$:Yb^{3+}, Er^{3+} is an energy transfer up-conversion (ETU) mechanism.[32] Under 980 nm excitation, the most likely emission mechanism is shown in Fig. 7. The electrons of Yb^{3+} are excited from ^{2}F$_{7/2}$ to ^{2}F$_{5/2}$ by absorbing phonon energy. Firstly, the Er^{3+} activator ions move from ^{4}I$_{15/2}$ to ^{4}I$_{11/2}$ through resonant energy transfer from Yb^{3+} to Er^{3+} via ET1: ^{2}F$_{5/2}$ (Yb^{3+}) + ^{4}I$_{15/2}$ (Er^{3+}) → ^{2}F$_{7/2}$ (Yb^{3+}) + ^{4}I$_{11/2}$ (Er^{3+}). Subsequently, ^{4}I$_{15/2}$ relaxes to the ^{4}I$_{13/2}$ level by non-radiation relaxation (NR), and the electrons of Er^{3+} are filled to the ^{4}F$_{9/2}$ level via ET2: ^{2}F$_{5/2}$ (Yb^{3+}) + ^{4}I$_{13/2}$ (Er^{3+}) → ^{2}F$_{7/2}$ (Yb^{3+}) + ^{4}F$_{9/2}$ (Er^{3+}). Then, the electrons transfer from ^{4}F$_{9/2}$ to ^{4}I$_{15/2}$, which generates red emission at 655 nm (Fig. 8a). Finally, the electrons at ^{4}F$_{9/2}$ are further populated to the ^{2}H$_{9/2}$ level via ET3: ^{2}F$_{5/2}$ (Yb^{3+}) + ^{4}F$_{9/2}$ (Er^{3+}) → ^{2}F$_{7/2}$ (Yb^{3+}) + ^{2}H$_{9/2}$ (Er^{3+}). In addition, the nonradiative transitions of Er^{3+} ions from ^{2}H$_{9/2}$ to ^{2}H$_{11/2}$/^{4}S$_{3/2}$ occur, which yields green emission at 529 nm (^{2}H$_{11/2}$ → ^{4}I$_{15/2}$) and 551 nm (^{4}S$_{3/2}$ → ^{4}I$_{15/2}$) (Fig. 8a).

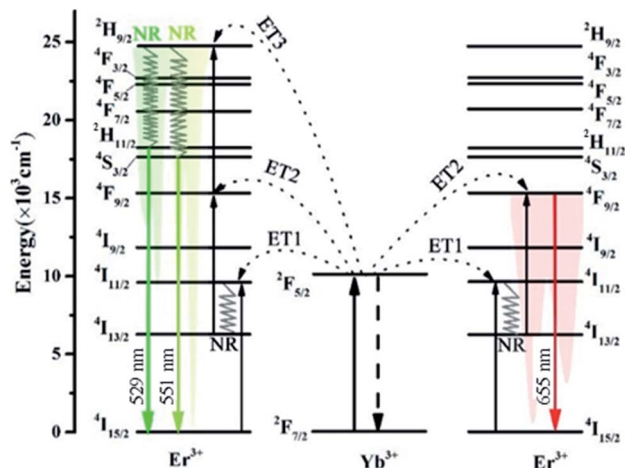**Fig. 7** Revealed energy transfer mechanism for the UC luminescence process of the NaLu(WO$_4$)$_2$:Yb^{3+}, Er^{3+} phosphor.

Fig. 8a depicts the UC emission spectrum (450–750 nm) of NaLu(WO$_4$)$_2$:Yb^{3+}/Er^{3+} phosphors in the range of 323–563 K. As the temperature increases, the fluorescence intensity changes significantly, especially at 529 and 551 nm. Due to the energy levels of ^{2}H$_{11/2}$ and ^{4}S$_{3/2}$ of Er^{3+} being close, the ΔE is less than 2000 cm^{-1}, which permits the upper level to fill from the lower level through rapid thermal population, resulting in the variation of the two thermal coupling states (TCSs).[33] The temperature dependence of the fluorescence intensity ratio (FIR) from ^{2}H$_{11/2}$ → ^{4}I$_{15/2}$ to ^{4}S$_{3/2}$ → ^{4}I$_{15/2}$ can be expressed as follows:[34]

$$\text{FIR} = \frac{I_H}{I_S} = C \exp\left(-\frac{\Delta E}{kT}\right) \quad \text{FIR} = \frac{I_H}{I_S} = Ce^{\frac{-\Delta E}{kT}} \tag{1}$$

here, I_H (529 nm) and I_S (551 nm) are the fluorescence intensities of ^{2}H$_{11/2}$ → ^{4}I$_{15/2}$ and ^{4}S$_{3/2}$ → ^{4}I$_{15/2}$, respectively; C is

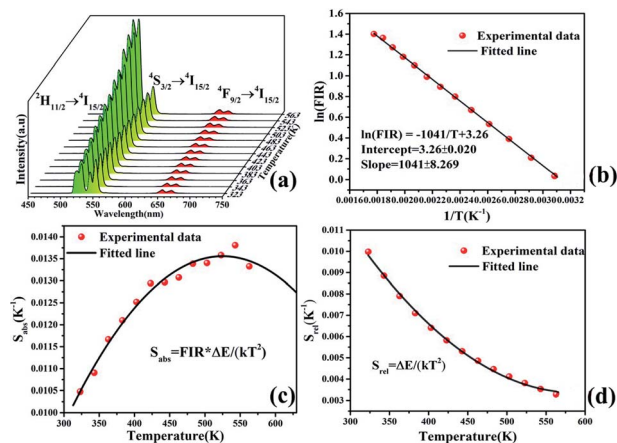**Fig. 8** (a) Emission spectrum of the NaLu(WO$_4$)$_2$:20%Yb^{3+}, 1%Er^{3+} phosphor under 980 nm excitation versus temperature from 323 to 563 K, (b) fluorescence intensity ratio of I_H/I_S, (c) absolute sensitivity (S_{abs}) and (d) relative sensitivity (S_{rel}).

a constant; ΔE is the energy difference between two adjacent thermal coupling energy levels; k is the Boltzmann constant and T is the absolute temperature. Fig. 8b describes the relationship between FIR (I_{529}/I_{551}) and $1/T$. The slope ($-\Delta E/k$) and intercept (ln C) obtained via linear fitting are -1041 and 3.26, and ΔE and C are further calculated to be approximately 723.1714 cm^{-1} and 26.0495, respectively.

As we all know, sensitivity is a crucial parameter that intuitively reflects the performance of temperature sensing. The absolute sensitivity (S_{abs}) is calculated using eqn (2)[35] and the relative sensitivity (S_{rel}) is calculated using eqn (3).[36]

$$S_{abs} = \left| \frac{\mathrm{dFIR}}{\mathrm{d}T} \right| = \mathrm{FIR} \times \frac{\Delta E}{kT^2} \tag{2}$$

$$S_{rel} = \left| \frac{S_{abs}}{\mathrm{FIR}} \right| = \left| \frac{1}{\mathrm{FIR}} \times \frac{\mathrm{dFIR}}{\mathrm{d}T} \right| = \frac{\Delta E}{kT^2} \tag{3}$$

Fig. 8c and d show the fitted curves of the relationship between S_{abs}, S_{rel} and T. The maximum value of S_{abs} is acquired to be 1.38% K^{-1} at 543 K and S_{rel} is $1041/T^2$. These values are similar to those of other Yb^{3+}/Er^{3+}-doped phosphors reported in the literature, as shown in Table 1. However, compared with a majority of the materials listed in the table, the temperature-sensitive parameters of NaLu(WO$_4$)$_2$:20%Yb^{3+}, 1%Er^{3+} are significantly larger. This indicates that the NaLu(WO$_4$)$_2$:20% Yb^{3+}, 1%Er^{3+} phosphor is superior to a majority of reported materials in the field of optical temperature measurement in the higher temperature range.

Fig. 9 is a comparison of the upconversion emission spectra of the nano-sample in our present work and the bulk sample according to a previous report.[11] Obviously, the position of the emission peak does not change, but the emission intensity is different. Although the upconversion luminescence intensity of the bulk sample is stronger due to its higher crystallinity and fewer surface defects, the upconversion luminescence intensity of the nano-sample also reaches 73% that of the bulk sample. Considering that the calcination temperature of the nano-sample is only 600 °C and the calcination temperature of the bulk sample is 1000 °C, the luminescence of the nano-sample is very good and can fully meet its practical application requirements. Furthermore, the synthesis temperature of our nano-
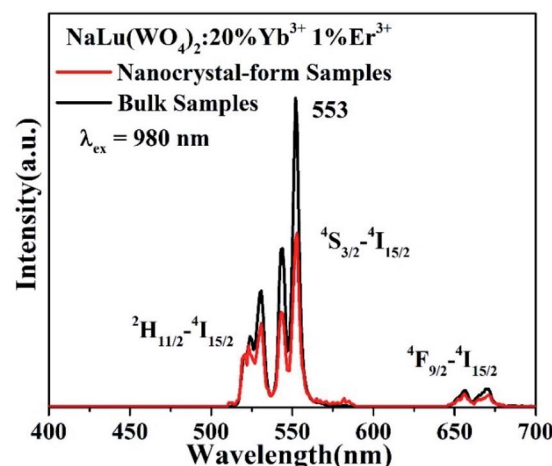

Fig. 9 A comparison of the upconversion emission spectra of the nano-sample in our present work and the bulk sample according to a previous report.[11]

samples is much lower than that of the bulk samples in the literature, providing the choice of a more environmentally friendly and energy-efficient synthetic method.[40–42]

Conclusion

In summary, we successfully prepared NaLu(WO$_4$)$_2$:Ln^{3+} phosphors via a hydrothermal method combined with subsequent calcination. Doping Ln ions with larger radii into the matrix causes the XRD diffraction peaks to shift to smaller angles. Under 980 nm near-infrared excitation, the NaLu(WO$_4$)$_2$:25% Yb^{3+}, 0.5%Tm^{3+} and NaLu(WO$_4$)$_2$:25%Yb^{3+}, 1%Ho^{3+} phosphors produced strong UC blue, green and red emission. Additionally, white UC emission with CIE-x = 0.3299 and CIE-y = 0.3293 was realized by 25%Yb^{3+}, 0.1%Ho^{3+}, 0.1%Tm^{3+} ions trip-doped into the NaLu(WO$_4$)$_2$ matrix. Besides, the obtained NaLu(WO$_4$)$_2$:20% Yb^{3+}, 1%Er^{3+} phosphor shows excellent temperature sensing performance with a maximum sensitivity as high as 1.38% K^{-1} at 543 K, which is better than that of many other previously reported temperature sensing materials. Thus, the NaLu(WO$_4$)$_2$:Ln^{3+} phosphors we obtained have potential applications in white lighting and optical temperature measurement.

Table 1 Comparison of temperature range and absolute sensitivity

Matrix	Temperature range (K)	Maximum S_{abs} (K^{-1})	S_{rel} (K^{-1})	Ref.
NaLu(WO$_4$)$_2$:Yb3+/Er^{3+}	323–563	1.38% (543 K)	1041/T^2	This work
NaGd(WO$_4$)$_2$:Yb^{3+}/Er^{3+}	298–383	1.2% (310 K)	1070/T^2	2
NaY(WO$_4$)$_2$:Yb^{3+}/Er^{3+}	293–503	0.9% (503 K)	1127/T^2	4
Lu$_2$TeO$_6$:Yb^{3+}/Er^{3+}	323–623	1.03% (623 K)	1241/T^2	33
NaGdF$_4$:Yb^{3+}/Er^{3+}	77–500	0.305% (298 K)	993.44/T^2	34
BaWO$_4$:Yb^{3+}/Er^{3+}	293–363	1.47% (393 K)	911.92/T^2	36
CaMoO$_4$:Yb^{3+}/Er^{3+}	303–873	1.43% (575 K)	1055.15/T^2	37
NaY(MoO$_4$)$_2$:Yb^{3+}/Er^{3+}	303–523	0.97% (493 K)	983.2/T^2	38
ZnWO$_4$:Yb^{3+}/Er^{3+}	83–583	0.99% (583 K)	1134.32/T^2	39

Conflicts of interest

There are no conflicts of interest to declare.

Acknowledgements

References

1 T. Guo, Y. Lin, W. J. Zhang, J. S. Hong, R. H. Lin, X. P. Wu, J. Li, C. H. Lu and H. H. Yang, *Nanoscale*, 2018, **10**(4), 1607–1612.

2 N. Yuan, D. Y. Liu, X. C. Yu, H. X. Sun, C. G. Ming, W. H. Wong, F. Yu, D. Y. Song, E. Pun and Y. B. Zhang, *Mater. Lett.*, 2018, **218**, 337–340.

3 Z. Wang, J. Zhong, H. Jiang, J. Wang and H. Liang, *Cryst. Growth Des.*, 2014, **14**(8), 3767–3773.

4 M. Lin, L. Xie, Z. Wang, B. S. Richards, G. Gao and J. Zhong, *J. Mater. Chem. C*, 2019, **7**(10), 2971–2977.

5 M. Yu, H. Xu, Y. Li, Q. Dai, G. Wang and W. Qin, *J. Colloid Interface Sci.*, 2020, **559**, 162–168.

6 X. Shi, M. S. Molokeev, X. Wang, Z. Wang, Q. Zhu and J. G. Li, *Inorg. Chem.*, 2018, **57**(17), 10791–10801.

7 Y. Zhang, X. Wang, H. Ye, X. Gong, Y. Li and X. Yao, *J. Mater. Sci.: Mater. Electron.*, 2018, **29**(23), 19840–19845.

8 Y. Zhai, Q. Sun, S. Yang, Y. Liu, J. Wang, S. Ren and S. Ding, *J. Alloys Compd.*, 2019, **781**, 415–424.

9 A. Nexha, J. J. Carvajal, M. C. Pujol, F. Díaz and M. Aguiló, *J. Mater. Chem. C*, 2020, **8**(1), 180–191.

10 E. W. Barrera, M. C. Pujol, J. J. Carvajal, X. Mateos, R. Sole, J. Massons, A. Speghini, M. Bettinelli and C. Cascales, *Phys. Chem. Chem. Phys.*, 2014, **16**(4), 1679–1686.

11 Z. Wang, J. Zhong, H. Liang and J. Wang, *Opt. Mater. Express*, 2013, **3**(3), 418.

12 Y. Huang, A. Skripka, L. Skripka, F. Sanz-Rodríguez, P. Haro-González, D. Jaque, F. Rosei and F. Vetrone, *Nanoscale*, 2018, **10**(2), 791–799.

13 G. Gao, D. Busko, S. Kauffmann-Weiss, A. Turshatov, I. A. Howard and B. S. Richards, *J. Mater. Chem. C*, 2017, **5**(42), 11010–11017.

14 R. V. Perrella and P. C. de Sousa Filho, *Dalton Trans.*, 2020, **49**(3), 911–922.

15 X. Zhu, J. Li, X. Qiu, Y. Liu, W. Feng and F. Li, *Nat. Commun.*, 2018, **9**(1), 2176.

16 A. R. N. Bastos, C. D. S. Brites, P. A. Rojas-Gutierrez, C. DeWolf, R. A. S. Ferreira, J. A. Capobianco and L. D. Carlos, *Adv. Funct. Mater.*, 2019, **29**(48), 1905474.

17 Y. Huang, A. Skripka, L. Labrador-Paez, F. Sanz-Rodriguez, P. Haro-Gonzalez, D. Jaque, F. Rosei and F. Vetrone, *Nanoscale*, 2018, **10**(2), 791–799.

18 A. Sedlmeier, D. E. Achatz, L. H. Fischer, H. H. Gorris and O. S. Wolfbeis, *Nanoscale*, 2012, **4**(22), 7090–7096.

19 Z. Wang, J. Christiansen, D. Wezendonk, X. Xie, M. A. van Huis and A. Meijerink, *Nanoscale*, 2019, **11**(25), 12188–12197.

20 A. Zhang, Z. Sun, G. Liu, Z. Fu, Z. Hao, J. Zhang and Y. Wei, *J. Alloys Compd.*, 2017, **728**, 476–483.

21 J. Sarkar, S. Mondal, S. Panja, I. Dey, A. Sarkar and U. K. Ghorai, *Mater. Res. Bull.*, 2019, **112**, 314–322.

22 B. Samanta, A. K. Dey, P. Bhaumik, S. Manna, A. Halder, D. Jana, K. K. Chattopadhyay and U. K. Ghorai, *J. Mater. Sci.: Mater. Electron.*, 2018, **30**(2), 1068–1075.

23 P. Xiao, S. Ye, H. Liao, Y. Shi and D. Wang, *J. Solid State Chem.*, 2019, **275**, 63–69.

24 A. L. Pellegrino, S. La Manna, A. Bartasyte, P. Cortelletti, G. Lucchini, A. Speghini and G. Malandrino, *J. Mater. Chem. C*, 2020, **8**(11), 3865–3877.

25 E. W. Barrera, M. C. Pujol, J. J. Carvajal, X. Mateos, R. Solé, J. Massons, A. Speghini, M. Bettinelli, C. Cascales, M. Aguiló and F. Díaz, *Phys. Chem. Chem. Phys.*, 2014, **16**(4), 1679–1686.

26 K. Cho, J. Choi, K. M. Kim, J. I Lee and J. H. Ryu, *Ceram. Int.*, 2015, **41**, S668–S674.

27 J. Méndez-Ramos, A. Santana-Alonso, A. C. Yanes, J. del-Castillo and V. D. Rodríguez, *J. Lumin.*, 2010, **130**(12), 2508–2511.

28 H. Xu, K. Xu, A. Lu, X. Wang and J. Hu, *J. Mater. Sci.: Mater. Electron.*, 2015, **26**(6), 3921–3925.

29 B. Zhao, D. Shen, J. Yang, S. Hu, X. Zhou and J. Tang, *J. Mater. Chem. C*, 2017, **5**(13), 3264–3275.

30 F. Wang, Y. Han, C. S. Lim, Y. Lu, J. Wang, J. Xu, H. Chen, C. Zhang, M. Hong and X. Liu, *Nature*, 2010, **463**(7284), 1061–1065.

31 D. Chen, Y. Yu, F. Huang, A. Yang and Y. Wang, *J. Mater. Chem.*, 2011, **21**(17).

32 H. Dong, L. D. Sun and C. H. Yan, *Chem. Soc. Rev.*, 2015, **44**(6), 1608–1634.

33 Z. Ma, J. Gou, Y. Zhang, Y. Man, G. Li, C. Li and J. Tang, *J. Alloys Compd.*, 2019, **772**, 525–531.

34 I. Mikalauskaite, G. Pleckaityte, M. Skapas, A. Zarkov, A. Katelnikovas and A. Beganskiene, *J. Lumin.*, 2019, **213**, 210–217.

35 X. Chai, J. Li, Y. Zhang, X. Wang, Y. Li and X. Yao, *RSC Adv.*, 2016, **6**(68), 64072–64078.

36 L. Xu, J. Liu, L. Pei, Y. Xu and Z. Xia, *J. Mater. Chem. C*, 2019, **7**(20), 6112–6119.

37 F. Huang, Y. Gao, J. Zhou, J. Xu and Y. Wang, *J. Alloys Compd.*, 2015, **639**, 325–329.

38 X. Yang, Z. Fu, Y. Yang, C. Zhang, Z. Wu, T. Sheng and A. Srivastava, *J. Am. Ceram. Soc.*, 2015, **98**(8), 2595–2600.

39 X. Chai, J. Li, X. Wang, Y. Li and X. Yao, *Opt. Express*, 2016, **24**(20).

40 L. Jiang and J. Yang, *Journal of Liaocheng University*, 2021, **34**(5), 21–26.

41 R. Ye and J. Yang, *Journal of Liaocheng University*, 2021, **34**(4), 37–42.

42 W. P. Xia, L. Jiang and S. S. Hu, *Journal of Liaocheng University*, 2020, **33**(5), 60–65.